

An investigation on the effect of deposition pattern on the microstructure, mechanical properties and residual stress of 316L produced by Directed Energy Deposition

*Original*

An investigation on the effect of deposition pattern on the microstructure, mechanical properties and residual stress of 316L produced by Directed Energy Deposition / Saboori, Abdollah; Piscopo, Gabriele; Lai, Manuel; Salmi, Alessandro; Biamino, Sara. - In: MATERIALS SCIENCE AND ENGINEERING A-STRUCTURAL MATERIALS PROPERTIES MICROSTRUCTURE AND PROCESSING. - ISSN 0921-5093. - ELETTRONICO. - 780:(2020), p. 139179. [10.1016/j.msea.2020.139179]

*Availability:*

This version is available at: 11583/2801860 since: 2020-03-10T17:57:46Z

*Publisher:*

Elsevier

*Published*

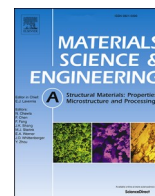
DOI:10.1016/j.msea.2020.139179

*Terms of use:*

This article is made available under terms and conditions as specified in the corresponding bibliographic description in the repository

*Publisher copyright*

(Article begins on next page)



# An investigation on the effect of deposition pattern on the microstructure, mechanical properties and residual stress of 316L produced by Directed Energy Deposition

Abdollah Saboori<sup>a,\*</sup>, Gabriele Piscopo<sup>b</sup>, Manuel Lai<sup>c</sup>, Alessandro Salmi<sup>b</sup>, Sara Biamino<sup>a</sup>

<sup>a</sup> Department of Applied Science and Technology, Politecnico Di Torino, Corso Duca degli Abruzzi 24, 10129, Torino, Italy

<sup>b</sup> Department of Management and Production Engineering, Politecnico Di Torino, Corso Duca degli Abruzzi 24, 10129, Torino, Italy

<sup>c</sup> IRIS S.r.l., Torino, Italy

## ARTICLE INFO

### Keywords:

Additive manufacturing  
Directed energy deposition  
Deposition pattern  
Microstructure  
Mechanical properties  
Residual stress

## ABSTRACT

In this work, 316L cubes were produced by Directed Energy Deposition (DED) process. To evaluate the effect of deposition patterns on the microstructure, mechanical performance and residual stress of 316L samples, two different deposition strategies are selected (67° and 90°). The general microstructure is revealed, and then the effect of deposition pattern on the microstructure of 316L alloy is evaluated through the Primary Cellular Arm Spacing (PCAS) analysis. The cooling rate in each sample is estimated according to the PCAS values. Interestingly, it is found that by increasing the rotation angle per layer, the PCAS value decreases as a consequence of increment in the cooling rate. On the other hand, in both cases, by increasing the distance from the substrate, due to the changes in cooling mechanisms, the cooling rate at first decreases and then at the last layers increases again. The phase composition analysis of 316L samples confirms the predictions that suggested the presence of residual  $\delta$ -ferrite in the final microstructure. In fact, the final microstructure of samples is characterized by austenitic dendrites together with some residual  $\delta$ -ferrite in the interdendritic regions. Moreover, the microstructural evaluations exhibit that during the DED process, some metallic inclusions are formed within the 316L samples that consequently deteriorates their mechanical properties. Tensile results show that the samples with 90° rotation per layer have a better mechanical performance such as slightly higher ultimate tensile strength and almost 35% higher elongation to fracture, mainly owing to their finer microstructure and slightly less oxide content. However, in both cases, the elongation of the 316L samples is lower than the typical elongation of this material produced via DED. This discrepancy is found to be as a result of higher inclusions contents in the samples produced in this work with respect to those of literature. Lastly, it is found that the residual stresses on the top surfaces are similar for both deposition patterns, although higher stress values are observed on the lateral surfaces of the cubes produce using the 90° rotation per layer.

## 1. Introduction

Additive Manufacturing (AM) technologies are recognized as new ways of production of three-dimensional (3D) metallic parts directly from Computer-Aided Design (CAD) model [1,2]. In fact, AM provides new possibilities in the world of design that allows new and optimized designs to be implemented in the production of complex-shaped parts that were not previously attainable [3,4]. Moreover, the rapid development of AM is because of its flexibility in the production of complex geometries, reduction of production time, eliminating the necessity of tooling and fixtures [5]. These advantages of AM make these

technologies promising in many industrial sectors from automotive, healthcare and mold tooling to aerospace [6]. In general, AM processes are classified into two broad categories: Powder Bed Fusion (PBF) processes and Directed Energy Deposition (DED) processes [7,8]. In PBF systems, a bed of powder is selectively melted by means of laser or electron beam heat source [8]. In contrast, ISO/ASTM 52900:2015 defines DED as 'an AM process in which a focused thermal energy is used to fuse materials by melting as they are being deposited' [9]. In fact, in this process, the starting materials, in the form of metallic powder or wire, are continuously delivered into the melt pool which is already generated by a focused thermal energy [10]. This feeding process continuous layer

\* Corresponding author.

E-mail address: [abdollah.saboori@polito.it](mailto:abdollah.saboori@polito.it) (A. Saboori).

<https://doi.org/10.1016/j.msea.2020.139179>

Received 3 January 2020; Received in revised form 26 February 2020; Accepted 28 February 2020

Available online 2 March 2020

0921-5093/© 2020 The Authors. Published by Elsevier B.V. This is an open access article under the CC BY license (<http://creativecommons.org/licenses/by/4.0/>).

by layer until a solid freeform component is built. In the literature, DED process has been recognized with different terminologies such as Laser Metal Deposition (LMD), 3D laser Cladding, Shaped Metal Deposition (SMD), Direct Metal Deposition (DMD), Direct Laser Deposition (DLD) and Laser Engineered Net Shaping (LENS) [10–13]. DED like the other AM technologies has its own unique advantages such as the possibility to produce the Functionally-Graded Materials (FGM) [14], repair of high-value parts [15] and surface coating of the components exposed to heavy loadings like die and moulds or harsh conditions like corrosive, erosive or wear [16]. In DED process, like the other AM technologies, a fully dense component can be produced by employing the optimal process parameters like laser power, laser scan speed, laser spot size, hatch spacing and z-step parameter [17,18]. Indeed, a complex thermal history that defines the incident energy and the geometry of the melt pool, is directly affected by the interaction among the process parameters [19,20]. Accordingly, this complex thermal history results in different microstructures and consequently, mechanical characteristics. As an example, high local energy and high laser scan speed lead to a large thermal gradient and also high cooling rates. Thereafter, these consequences lead to the generation of complex hydrodynamic fluid flows and accordingly change markedly the crystal growth, orientation, microstructural defects and finally melted particles [21].

The dynamic nature of thermal phenomena in DED processes induces a large amount of residual stresses. These residual stresses are developed from the reiteration of heating/cooling cycles and from the high-temperature gradient that occurs during the process. Moreover, it was observed that the thermal misfit between two adjacent regions highly influence the residual stresses in DED based processes [22].

Dai and Shaw and Nickel et al. using a finite element model analysis showed that the residual stresses and the related distortions were significantly dependent on the laser deposition pattern. Using a bi-directional deposition strategy elongated along a direction, the resulting distortion was characterized by a saddle shape. The distortion was reduced by varying the laser deposition pattern. In fact, using an offset-out deposition strategy the induced distortion was minimized to about 1/3 with respect to the distortion obtained using the first deposition pattern [23,24].

Some fundamental characteristics of the produced components such as tensile and fatigue resistance, i.e. the integrity and the lifetime of components, are influenced by the presence and the amount of residual stresses [25]. Due to their importance, it was vital to develop the different tools and methods that allowed to estimate the amount of residual stresses in the components. From an industrial point of view, the hole drilling strain gauge method is one of the most interesting method used to measure stresses in a component with respect to the depth method [26]. This method is characterized by unique capabilities such as good accuracy and reliability and it has a standardized procedure. For these reasons this method is widely used for residual stress measurement on samples produced by AM processes [27–30].

Over the past two decades, austenitic stainless steel is one of the most promising materials that has been processed by the DED process [31–33]. Its good mechanical properties, together with excellent corrosion and excellent processability, make 316L stainless steel a promising alloy to be widely used in different industrial sectors from the automotive to petrochemical applications. In the production of large complex shape 316L components, DED process is considered as the most interesting techniques that can provide a high grade of feasibility in the design and production. In fact, through this feature of this technology, it would be possible to reduce the weight, increase the saving of the expensive materials, and thus limit the need for costly machining steps.

A considerable amount of literature has been published on the correlation between the process parameters and the mechanical properties of 316L components fabricated via DED process [18,34–36]. For instance, Yadollahi et al. investigated the effect of the time interval between the deposition of layers on the mechanical performance of 316L [37]. According to their results, by increasing the time interval, the

cooling rate increases and consequently results in the formation of a finer microstructure, higher strength and lower elongation. Zietala et al. studied the effect building direction of the mechanical performance of 316L components produced via DED process [36]. They found that the lowest Yield Strength (YS) and Ultimate Tensile Strength (UTS) were achieved in the samples produced in the perpendicular direction of the building direction mainly owing to the presence of a high quantity of the processing pores at the interlayers. Ma et al. studied the correlation between the mechanical properties of 316L and the size of Primary Cellular Arm Spacing (PCAS) [38]. According to their findings, at high laser energy densities, larger PCASs are formed that consequently result in lower mechanical performances. In another work, Wang et al. investigated the effect of a pulsed laser on the characteristics of the components produced via DED [39]. It is stated that low inputted energy results in high cooling rates and very fine microstructure that increase the mechanical strength of the 316L parts. Recently, Saboori et al. evaluated the effect of powder recycling on the microstructure and mechanical properties of the 316L components produced by DED process [40]. According to their results, it is found that the parts made of 316L produced via DED process by using fresh and recycled powder behave markedly different, in particular in terms of elongation. In fact, it is revealed that the elongation of the parts using fresh power is 50% higher than those produced using recycled powder as a result of a lower inclusion content. Nevertheless, neither of referred works considered the effect of deposition pattern on the microstructure, mechanical properties and residual stresses of the 316L components produced by DED process. To date, this aspect remains unstudied and from the industrial point of view, there would be an urgent need to understand this aspect to minimize the post-processing cost for stress relieving and also increase the mechanical properties of the parts, simply by changing the deposition pattern. Hence, this work is aimed at better understanding the effect of deposition pattern on the microstructure, mechanical properties and residual stresses of the 316 DED samples.

## 2. Materials and methods

### 2.1. Starting material

A gas atomized, pre-alloyed 316L powder with the particle size range of 44–106  $\mu\text{m}$  which was supplied by LPW technology Ltd was used as starting material ( $d_{10} = 51.4 \mu\text{m}$ ,  $d_{50} = 71.2 \mu\text{m}$ ,  $d_{90} = 91.3 \mu\text{m}$ ). Table 1 shows the chemical composition of as-receive 316L powder which is in line with the 316L powder employed in previous works [41,42].

The morphology and the cross-section of the starting 316L powder are shown in Fig. 1 (a–b). As can be seen in this figure, the majority of the particles are spherical with rather smooth surfaces and exhibit the satellites which are a typical defect that can be revealed in the gas atomized powders. In addition to the spherical particles, few irregular particles are found in the batch of powder. The cross-section analysis of the powder also confirms the presence of internal porosity in a few particles that can be formed during the atomization process (red arrows in Fig. 1 (b)). The oxygen content of starting 316L powder and massive samples was evaluated using the inert gas fusion method via LECO ONH836 Oxygen/Nitrogen/Hydrogen elemental analyzer. Carbon and sulfur content were also analyzed via infrared absorption carbon-sulfur analyzer (LECO CS844).

### 2.2. Experiments

In this work, depends on the type of analysis two types of samples were produced: bar ( $20 \times 20 \times 100 \text{ mm}^3$ ) for tensile test and cube ( $20 \times 20 \times 20 \text{ mm}^3$ ) for microstructure and residual stress analyses. The production of specimens was performed using an IRB 4600 machine from ABB robotics with 3 kW fiber laser equipped with a 4-way nozzle. Argon with 99.99% purity was used as the carrier gas and shield gas in this work. 316L plates of  $100 \times 100 \times 8 \text{ mm}^3$  were used as a substrate.

**Table 1**  
The standard and nominal chemical composition of AISI 316L stainless steel powder.

Composition (wt.%)	C	Si	Mn	Cr	Mo	Ni	Cu	Fe
Standard	0.03	0.75	2.00	16.00–18.00	2.00–3.00	10.00–14.00	0.75	Bal.
Nominal	<0.01	0.54	0.76	17.70	2.28	12.60	0.02	Bal.

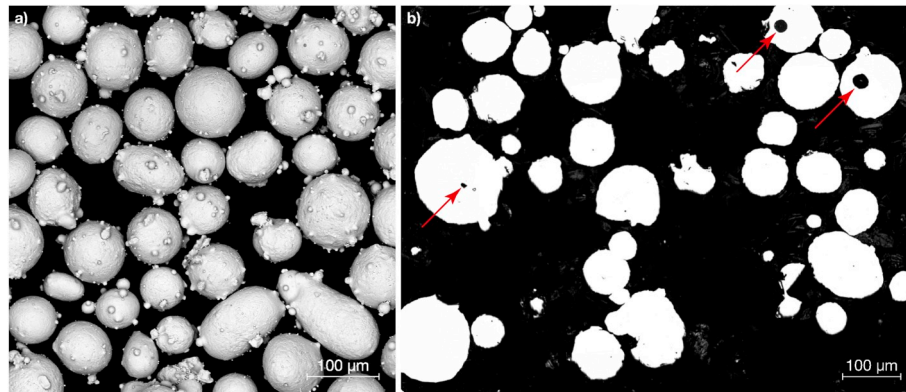


**Fig. 1.** (a) Morphology, and (b) cross-section of the starting 316L powder.

Prior to the deposition, each substrate was entirely cleaned and degreased with ethanol. All the samples were produced using a specific combination of process parameters which is listed in Table 2. Moreover, two different deposition strategies were used for the production of samples: 0–90° which is an orthogonal deposition direction between two layers (coded as 0090), and 0–67° which is a 67° rotation for each new layer (coded as 0067).

### 2.3. Characterizations

For microstructural analysis, the cubes were cut along the building direction from the central part. Thereafter, their cross-section was polished using the standard metallography procedure to achieve a mirror-like surface. Afterwards, in order to reveal the microstructure of 316L cubes, they were immersed for 9 s in a solution of 15 mL HCl + 10 mL HNO<sub>3</sub> + 1 mL acetic acid. A LEICA DMI 5000 M Optical Microscope (OM) (Leica microsystems, Germany) and a Merlin Zeiss Supra TM 40 Field Emission Scanning Electron Microscope (FESEM) (Zeiss International, Germany) equipped with an EDS analysis system were employed for the microstructural analysis. Several images at the different distances from the substrate (every 5 mm) were acquired to estimate the cooling rate values according to the PCAS measurements. The PCAS values were measured at every 5 mm from the substrate according to the triangle method [38]. According to the triangle method, the average distance of the central parts of the three adjacent cellular dendrites is considered as PCAS. Form the statistical point of view, each PCAS is reported as an average of 50 measurements. Indeed, at each distance from the substrate at least 5 images from the left to right side along the X/Y direction were acquired and then 10 measurements were carried out on each image.

X-ray diffraction (XRD) analysis was implemented on a representative sample of each deposition pattern to investigate their phase composition. The XRD analysis was carried out using an X-Pert Philips (Malvern Panalytical, United Kingdom) diffractometer (Cu-K $\alpha$ ) in a Bragg

Brentano configuration in a 2 $\theta$  in the range of 30–100° with step size and time per step of 0.013° and 35 s, respectively.

In order to prepare the samples for the tensile test, at first, the as-built rectangular bars with the dimension of 20 × 20 × 100 mm<sup>3</sup> were removed from the substrate. Thereafter, the flat tensile samples were machined according to ASTM-E8 standard with 4 mm thickness. For each deposition pattern, three samples were machined, tested and the average results were reported as the mechanical properties. The tensile tests were carried out using a Zwick Z100 testing system (Zwick Roell, Germany) with a strain rate of 8 × 10<sup>-3</sup> s<sup>-1</sup>. After the tensile test, the fracture surfaces were analyzed using FESEM.

The residual stress behaviour beneath the surface was evaluated using the semi-destructive hole drilling strain gauge method, according to ASTM E837-13a [43]. The RESTAN MTS3000 (SINT Technology S.r.l., Italy) system was used. To optimize the adhesion between the analyzed surface and the rosette it was necessary to prepare the surface in order to obtain a roughness of about 4 μm. Thus, agglomerated particles were removed using a flat, high carbon, steel file and the surface was then ground using abrasive paper with different grain dimensions (120, 400 and 600 grit). A 1.6 mm diameter drill bit was used in the experimental procedure to produce a 1.2 mm deep flat-bottom hole, by executing 24 drilling steps to a depth of 50 μm. The strain released at each measurement step was acquired using the RMS software (SINT Technology S.r.l., Italy). Using this software, it was possible to accurately control the drill bit feed rate. Then, the acquired strains were introduced into EVAL (SINT Technology S.r.l., Italy) software to back-calculate the residual stresses in compliance with the ASTM E837-13a standard. Due to dynamic nature of the DED process, the stresses were calculated assuming a non-uniform distribution of residual stresses. The measurements were performed on the top surface and on the lateral side. In particular, due to the symmetry of the deposition pattern used in this test, the side selected for residual stress measurement are Side A and Side B, as depicted in Fig. 2. In the following paragraphs, the cubes produced with the 0–90° and with the 0–67° deposition strategy are named C-0090 and C-0067, respectively. Fig. 3 schematizes the arrangement of the strain gage rosette on the analyzed surfaces.

**Table 2**  
Process parameters used in this work.

Laser Power, P	Laser speed, v	Laser Focus, h	Powder feeding rate	Carrier gas flow rate	Overlap in X	Overlap in Z
900 W	15 mm/s	7.5 mm	3.5 rpm	5 L/min	50%	25%

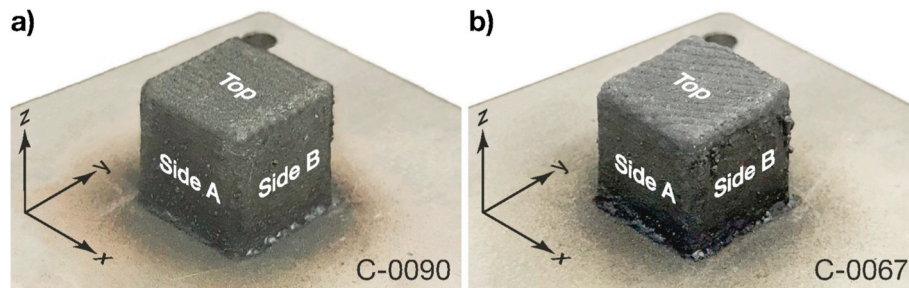


Fig. 2. Identification of Top surface, Side A and Side B on sample (a) C-0090 and (b) C-0067.

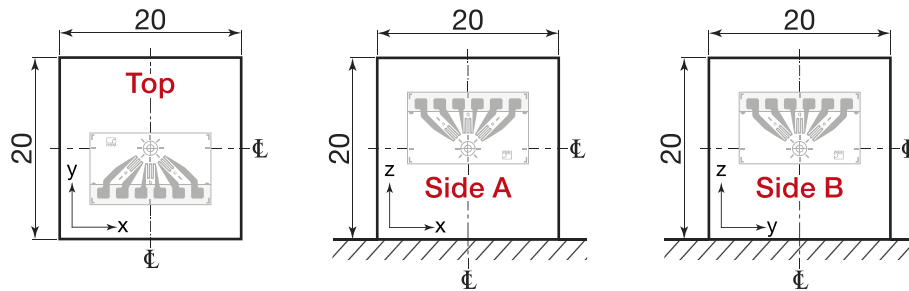


Fig. 3. Arrangement of the strain gage rosette on the cubic sample.

### 3. Results and discussions

#### 3.1. Microstructure

A representative cross-section of the as-built 316L C-0067 and C-0090 samples, after polishing down to  $1\ \mu\text{m}$  are shown in Fig. 4(a–b). It is important to notice that based on OM results, both samples have a nearly dense structure and no process-induced porosity is found in those samples. However, it is revealed that in both cases the samples contain some spherical inclusions. A more in-deep analysis of these inclusions by means of FESEM-EDS mapping shows that they are mainly oxides rich in Si or Si/Mn that can adversely affect the mechanical properties of the material (Fig. 5).

As can be seen in Fig. 5, the coarse oxides with an average diameter of  $3.4 \pm 1.6\ \mu\text{m}$  are rich in Si and Mn, whereas the finer ones with an average diameter of  $0.8 \pm 0.5\ \mu\text{m}$  are rich only in Si. The presence of these spherical oxides is the product of a re-oxidation of the alloying elements that is normally found during ladle practice of highly containing Mn/Si steels [44–46]. In fact, it is believed that because of the

high reactivity of Si and Mn, from the thermodynamic point of view, the oxidation of those elements is hardly avoidable even during the secondary steelmaking process. Thus, the formation of these oxides despite using a shielding gas to limit the direct contact of the atmosphere with the molten material was expectable.

Thereafter, both 316L cubes produced using two different deposition patterns were chemically etched to investigate their microstructures more in details.

Substantially, in DED process, morphology and grain size which are two main microstructural features of 316L alloy can be defined depends on the thermal history of the specimen during the production process. High solidification rate, significant thermal gradient and bulk temperature increment are the key factors that define the final microstructure of the alloy. Notwithstanding these parameters and their effects, the prediction of the microstructure of an alloy produced via DED based on the involved process parameters is still a challenge. Basically, a combination of parameters such as the travel speed of liquid/solid interface ( $R$ ), the temperature gradient ( $G$ ), the undercooling and the composition of material determines the microstructural features. Specifically, the

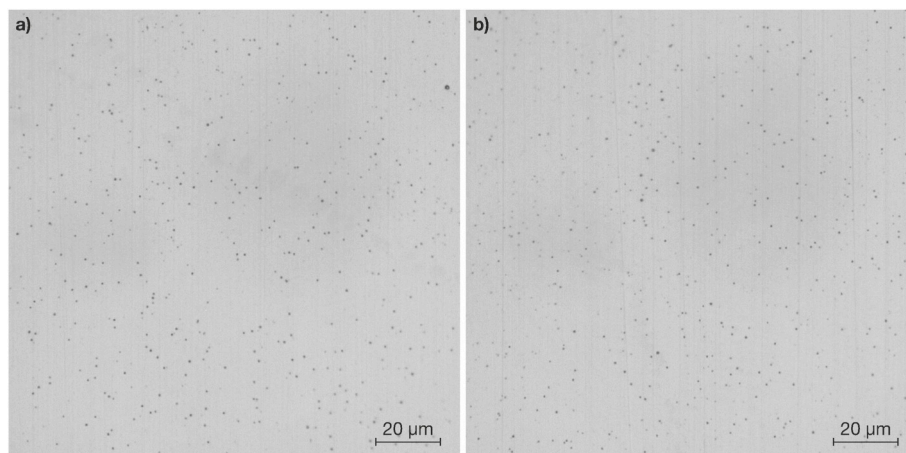


Fig. 4. OM images of the cross-section of 316L cube produced via DED (a) C-0090, and (b) C-0067.

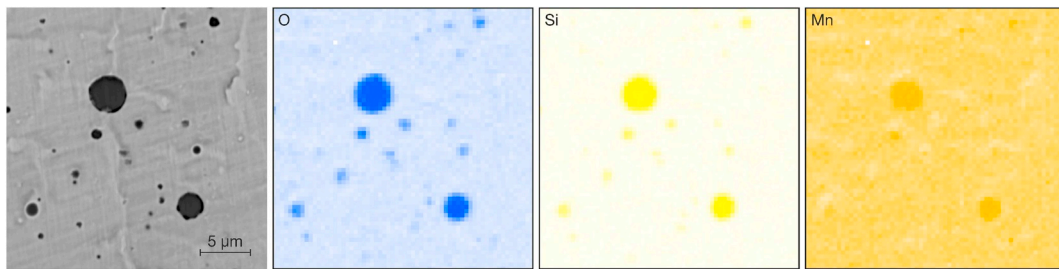


Fig. 5. SEM-EDS mapping of the cross-section of 316L C-0090 sample confirming the presence of inclusions in the as-built microstructure.

cooling rate levels ( $G \times R$ ) define the scale of microstructure and  $G/R$  ratio defines the solidification mode, and accordingly, the microstructural characteristics [47,48].

Microstructure refinement is one of the direct consequences of the high cooling rate in the DED process ( $10^3$ – $10^4$  K/s) that has a positive effect on the mechanical performance of each material. However, it should be noted that local change in the  $G$  and  $R$  values results in the formation of different microstructures, such as equiaxed or columnar, in the as-built 316L alloy. Fig. 6 shows a representative OM microstructure from different positions of 316L C-0090 sample: from the last layer, two positions from the central part and the interface between the deposited cube and substrate. As can be seen in Fig. 6 (a), on the external surface of the 316L cube a thin layer of oxide ( $23 \pm 4.3 \mu\text{m}$ ) is formed. In addition, some unmelted particles are found on the top surface that contributes markedly in the surface roughness of the as-built 316L cubes. Moreover, it is revealed that in the last deposited layer a cellular structure is dominated after a columnar structure which is dominated in the central part the sample as an effect of a complex heat transfer during the DED process. Fig. 6 (b) exhibit a columnar and equiaxed growth of dendrite structures in a macro defect-free sample. From this figure, the transition between the layers is clearly visible. An epitaxial grain growth toward the maximum thermal gradient in the middle height of the sample is completely visible in Fig. 6 (c). Furthermore, the curved borders of melt pools are detectable in the microstructure which is as a direct consequence of the Gaussian distribution of laser energy. A defect-free

interface of the cube and substrate is shown in Fig. 6 (d). In addition to a defect-free interface, the Gaussian distribution of laser energy is also noticeable. The presence of this kind of interface confirms also the great potential of this technology to repair the high value and semi-complex 316L industrial parts.

The presence of a complex thermal regime during the DED process as well as the mechanism of a melt pool and a Heat Affected Zone (HAZ) formation is described elsewhere [49,50]. As far as the whole section of melt pool is concerned, it is revealed as a consequence of different heat transfer mode in HAZ, central zone and border of a melt pool, different microstructures are formed. Indeed, in the border of a melt pool, where the lateral sides of the melt pool are in contact with the working atmosphere, the heat transfer mode is a mix of conductive-convective-radiation mechanisms, whereas in the central part, where the liquid metal solidifies with delay, the heat transfer mode is convective. These discrepancy in the heat transfer modes that result in a complex microstructure feature (columnar growth from the melt pool border toward its central part that has an equiaxed structure) are observable in Fig. 6 (d). These solidification modes imply that within the melt pool along the orthogonal direction with respect to its border, the temperature gradient is rather high that leads to an oriented growth. Instead, in the central part of the melt pool the heat transfer is not as high as its borders and, thus results in heat transfer with random orientation and consequently formation of equiaxed dendrites. On the other hand, it should be highlighted that a uniformly heated substrate

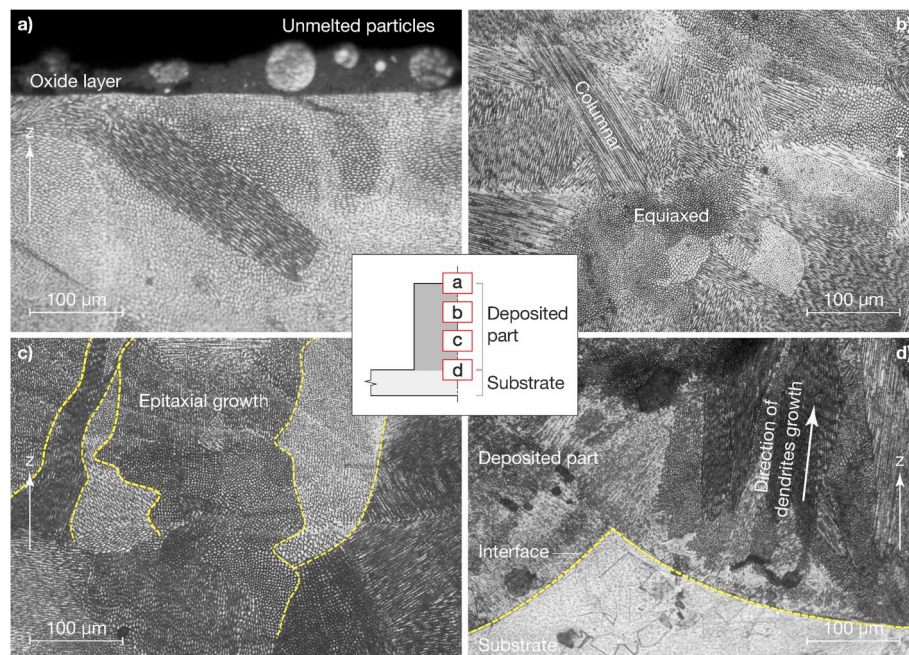


Fig. 6. OM micrographs of the 316L stainless steel sample produced via DED process using  $90^\circ$  rotation strategy: (a) the cross-section of the oxide layer and unmelted particles remained on the top surface of the 316L cube, (b) a representative microstructure of 316L cube including equiaxed and columnar features (c) a representative microstructure of 316L cube showing the epitaxial grain growth during the DED process, (d) the interface between the substrate and deposited cube.

plays a key role in the cooling rate and accordingly the microstructure of the first layer which is in direct contact with the substrate. However, by increasing the distance from the substrate the role of the substrate is less effective. This change in the role of the substrate as a heat sink is mainly owing to the change of heat sink player, from the substrate to the previously deposited layers, for the subsequent layers. It implies that the cooling rate may change with the height of deposition that accordingly results in different microstructures.

The effect of deposition pattern (67° and 90° rotation per layer) on the microstructural features, which is one of the aims of this work is also considered and analyzed. Interestingly, it is found that the general microstructural features such as epitaxial growth of the columnar grains on the opposite direction of heat flux, presence of equiaxed microstructure in the last layer and presence of the curved melt pool borders in the microstructure are almost identical. However, it is found that the microstructure of the C-0090 samples is slightly finer than C-0067 sample. This discrepancy in those microstructures could be related to a change in their thermal history during the deposition process. As a consequence, this variation in thermal history could result in different thermal gradients and cooling rates during the solidification phase. Therefore, a finer microstructure for the sample that is subjected to a higher cooling rate could be expected. To estimate the cooling rate during the deposition process of two different specimens using various deposition patterns, the PCAS at different distances from the substrate and its total average value was measured. As described earlier, at every 5 mm distance from the substrate at least 5 images from the left to right side along the X/Y direction were acquired and then 10 measurements were carried out on each image to consider all the different PCAS sizes in the calculations. Fig. 7(a–b) are the representative images of DED 316L at 10 mm from the substrate. Fig. 7 (a) shows a representative of the C-0090 sample, whereas Fig. 7 (b) illustrate the one regarding the C-0067 sample. As can be seen in these figures, the cell size in the C-0090 sample is slightly finer than that observed in the C-0067 sample. Fig. 8 (a) shows the PCAS values of these samples as a function of distance from the substrate. From the chart, it can be seen that in both cases by increasing the distance from the substrate up to 15 mm, the PCAS values increases markedly. Thereafter, nearby the last layers, a sudden drop in the PCAS values are revealed. Nonetheless, from the graph, we can see that the PCAS values for the C-0067 samples are slightly higher than those observed on the C-0090 samples. This finding is perfectly in line with the microstructure observations that are presented in Fig. 7(a–b). In addition, it is found that the variation in the PCAS values and the standard deviations for the C-0067 samples is not as significant as those for the C-0090 samples. This different behaviour in the variation of PCAS values for these samples can be related to the different thermal history that

those samples were experienced during the DED process. Therefore, it can be expected that these different thermal histories lead to the different cooling rates and accordingly different PCAS values.

Kim et al. [51] and Yin et al. [52] reported that the cooling rate during the solidification is the main affecting parameter on the PCAS value and this relationship can be quantified through the following equation:

$$\lambda_1 = 80\dot{T} - 0.33 \quad (1)$$

Where  $\lambda$  is PCAS,  $\dot{T}$  is the cooling rate. According to the literature, this equation is the most useful equation that can be successfully employed to evaluate the correlation between the PCAS and the cooling rate for different stainless steels [38,40,53]. Hence, in this work, this equation is also employed to estimate the cooling rate at different distances from the substrate and the results are shown in Fig. 8 (b).

As it is shown in Fig. 8 (b), the cooling rate in both cases decreases by increasing the distance from the substrate. In fact, in the sample C-0067 sample, by increasing the height of sample up to 15 mm the cooling rate decreases from  $1.13 \times 10^4$  to  $4.47 \times 10^3$  K/s and thereafter at the last layers raised again up to  $4.85 \times 10^3$  K/s. As same as these cubes, in the case of the C-0090 sample the cooling rate decreases from  $2.05 \times 10^4$  K/s down to  $5.18 \times 10^3$  K/s when the deposition height increases from 5 to 15 mm. Even in this case a slight increase in the cooling rate is achieved (it reached  $1.24 \times 10^4$  K/s). In both cases, the first decreasing trend can be related to the decreasing role of the substrate as a heat sink, the heat accumulation as a consequence of the subsequent depositions and also decreasing the thermal gradient by increasing the distance from the substrate. Instead, in the last layers, in which there is no further deposition, the sample remains in direct contact with the deposition atmosphere and therefore the heat dissipation can be enhanced via increased radiative surface. This variation in the heat dissipation mechanisms can clearly explain the difference in the cooling rate and consequently the PCAS value from the bottom to the top of each cube. However, it should be noticed that the variation of cooling rate in the case of deposition with 67° rotation per layer is less obvious and this can be ascribed to higher heat accumulation during the DED process of these samples that results in a lower thermal gradient and cooling rate variation. In addition, the average cooling rate for both cubes (using 67° and 90° rotation per layer) is calculated and it is found that this value for the C-0067 and C-0090 samples is  $6.71 \times 10^3$  K/s and  $1.16 \times 10^4$  K/s, respectively. As can be seen, the average cooling rate for the C-0067 sample is almost 40% lower than that of C-0090 sample, and as a consequence a coarser microstructure is expected for this sample. It is interesting to highlight that in both cases the calculated cooling rate is in a good agreement with previous works [38,40,54,55].

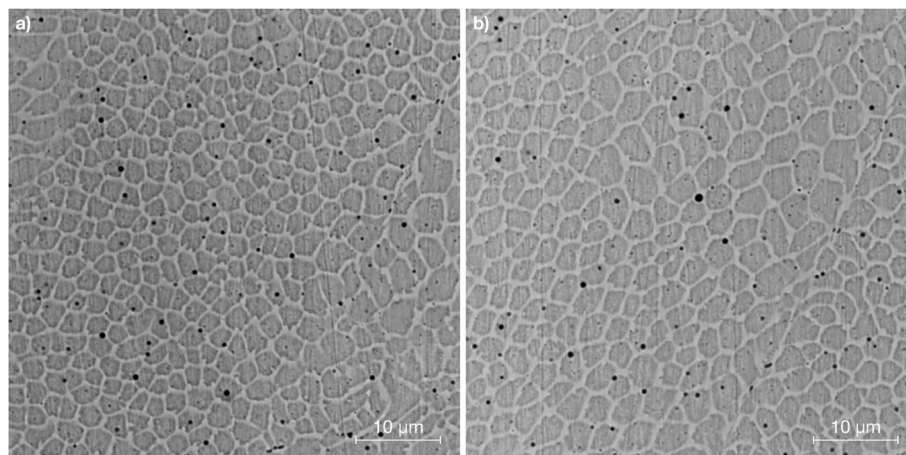
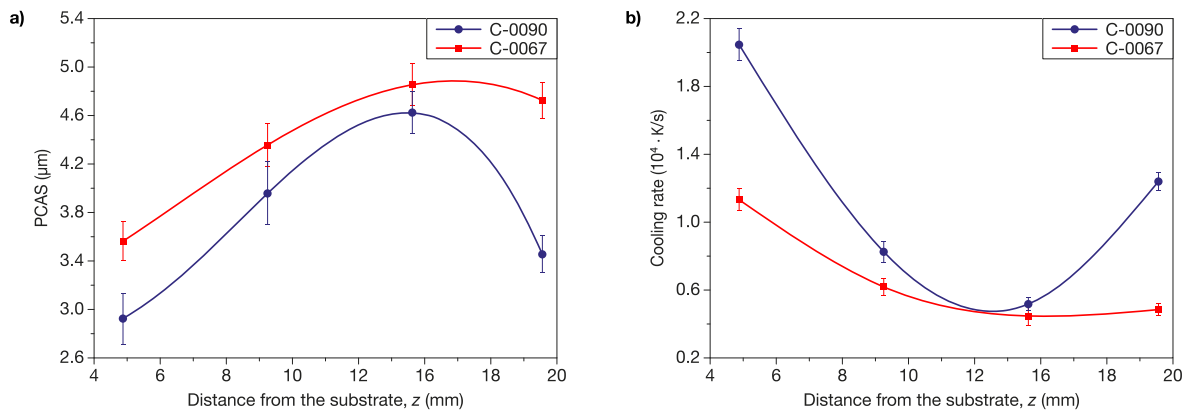


Fig. 7. A representative images for the cubes deposited with (a) 90°, and (b) 67° rotation per layer that is considered in the PCAS evaluations (at 10 mm from the substrate).



**Fig. 8.** (a) PCAS, (b) cooling rate as a function of the distance from the substrate for the DED 316L cubes produced by 90°, and 67° rotation per layer as the scanning patterns.

On the other hand, this high cooling rates during the DED process derives the development of the as-built microstructure of the cubes. According to literature, in a standard rapid solidified austenitic stainless steel, two different microstructures, based on its chemical composition, are achieved: austenite ( $\gamma$ ) and  $\delta$ -ferrite [56]. In DED process, due to the presence of high cooling rates which is usually higher than those in the conventional production processes, the solidification process is out of equilibrium state. Therefore, to predict the theoretical gross content of  $\delta$ -ferrite, a Schaeffler diagram and a Pseudo-binary predictive phase diagram which are presented in the previous works [57] are also used. According to these diagrams and using equivalent contents of Cr and Ni that can be calculated according to the equations which are reported elsewhere [40,57], it is found that the theoretical gross content of  $\delta$ -ferrite lies in the range of 5–10%. In the current research, the values of  $Cr_{eq}$  and  $Ni_{eq}$  are calculated based on the chemical composition of the starting powder and their ratio was calculated to be 1.498 (Table 1). Thereafter, in order to analyze the phase composition of the as-built 316L cubes, XRD analysis was carried out and its patterns regarding the 316L samples produced by different deposition patterns are presented in Fig. 9.

As can be seen in Fig. 9, there are two main differences in the XRD patterns of the cubes deposited by different deposition strategies. The first difference is related to the presence of a small peak at the angle of 44.7° in the XRD pattern of the C-0090 sample, whereas, in the other one, there is no peak at the position. In fact, this discrepancy suggests the presence of a higher quantity of the residual  $\delta$ -ferrite in the final microstructure of this sample. As discussed earlier, in DED process with

90° rotation per layer as deposition pattern the material solidifies with higher cooling rate (with respect to the C-0067 sample) that results in the consumption of austenite stabilizer elements such as Ni, C and N. As a consequence, an intense partitioning of alloying elements happens and the residual liquid fraction becomes rich in ferrite promoting elements. Instead, in the case of 67° rotation per layer, as it is found earlier, the cooling rate is lower and the solidification is slightly closer to the equilibrium condition. This lower cooling rate can reduce the level of the partitioning of alloying elements, and therefore lower residual  $\delta$ -ferrite can be expected in this sample. It should be noticed that an accurate determination of the partitioning coefficients of the different alloying elements in these conditions is rather difficult. However, in the literature, it is believed that when 316L alloy is welded or laser-treated, the last fraction of liquid metal enriched in  $\delta$ -stabilizers such as Mo, Si, and Cr [58,59]. Another difference in the XRD patterns of the cubes produced with different deposition patterns is related to their peaks intensities. This difference can also be as a consequence of the different thermal histories of the samples that led to the different thermal gradients and consequently in diverse textures in those samples. This finding is also in line with previous works [18].

### 3.2. Mechanical properties

In order to investigate the correlation between the deposition pattern and mechanical properties of 316L alloy produced via DED process, tensile tests were carried out on the bar samples deposited using two

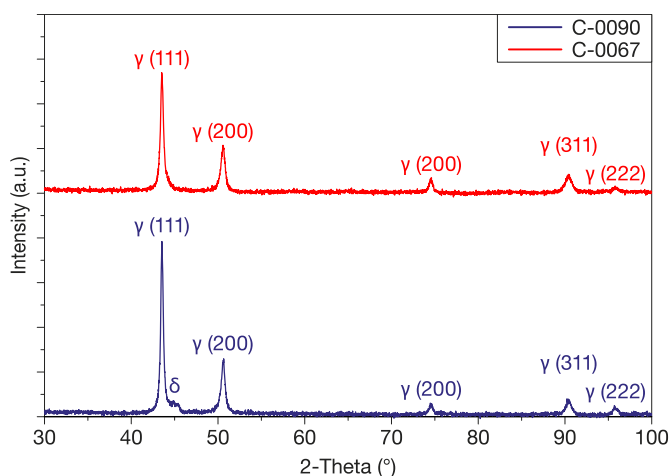


**Fig. 9.** X-ray diffraction pattern of as-built AISI 316L samples using two different deposition patterns.

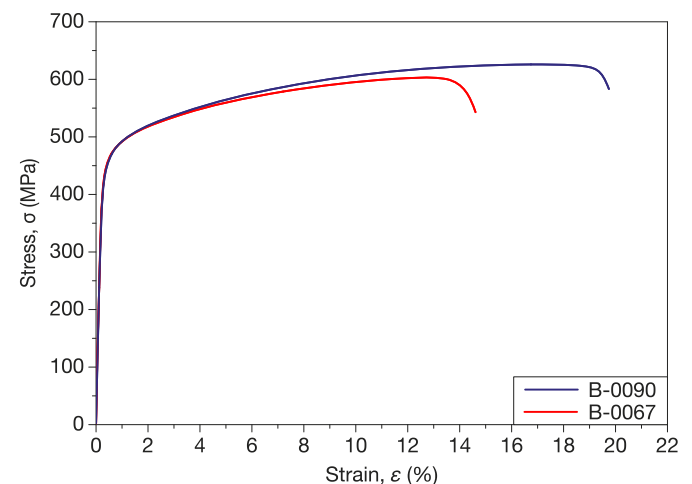


**Fig. 10.** Stress-strain curves of AISI 316L produced by DED using 67° and 90° rotation per layer as deposition pattern.

different deposition patterns: 67° and 90° rotation per layer (Fig. 10). These samples are named B-0067 and B-0090, respectively.

Fig. 10 shows that the tensile behaviour of the DED 316L samples produced by different deposition patterns is markedly different, in particular, their elongation to fracture. However, as can be seen in the graph, their work-hardening behaviour is the same for both samples. Indeed, it is clear that the Ultimate Tensile Strength (UTS) and elongation to fracture ( $\epsilon_r$ ) of the B-0090 sample are 7% and 27%, respectively, higher than those measured on B-0067 sample. Moreover, it is found that in the stress-strain curves of both cases a sudden drop, exactly after reaching the UTS, is taken place. This sort of deformation behaviour is normally revealed in the composite material where there is some second phases are present in a metallic matrix as a reinforcement [60]. In the current work, this aspect can be ascribed to the presence of inclusions (oxides rich in Si and Si/Mn), as they are revealed in the as-built microstructures (see in Fig. 5). Indeed, these inclusions decrease the maximum capacity of the material to be plastically deformed and consequently decrease the elongation of the 316L sample.

Fundamentally, it is expected that these inclusions provide a dispersion strengthening effect on the 316L samples and improve their mechanical properties [61,62]. Surprisingly, it is found that the presence of these oxides not only reduce the elongation of the alloy but also does not have any strengthening effect. This deleterious effect can be related to the following reasons: the size and distribution of these oxides. According to the strengthening rules, by increasing the size of the second phase the strengthening efficiency decreases and it implies that, in this work, the size of inclusions is larger than the effective threshold, and thus they have no contribution in the strengthening of 316L alloy [63]. On the other hand, since the DED process is not a controlled dispersion strengthening process, the distribution of oxides within the 316L matrix is definitively not uniform and consequently cannot participate in the strengthening of the 316L samples.

Nonetheless, as it can be seen in Fig. 10, the mechanical performance of the B-0090 samples is higher than obtained on B-0067 samples. This slight discrepancy can be explained by their microstructure and inclusion content. As discussed earlier, a different thermal history of the cubes results in different cooling rates, microstructure and oxide content (see Fig. 8). As a matter of fact, it is revealed that by decreasing the angle of rotation per layer from 90° to 67°, the cooling rate decreases and results in the formation of coarser microstructure. Therefore, better mechanical performance for the samples with a finer microstructure was expected. Moreover, the evaluation of inclusion content by image analysis indicated that the oxide content in the B-0067 sample is  $1.52 \pm 0.65\%$ , which is almost 20% higher than the oxide content in the B-0090 sample ( $1.27 \pm 0.36\%$ ). To verify the oxygen content of the samples, both samples were analyzed by means of the inert gas fusion technique. The results of this analysis show that the oxygen content of the B-0067 and B-0090 samples is 1985 and 1600 ppm, respectively. It is interesting to note that, according to both oxide content analysis and oxygen

content evaluations findings, the deposition pattern can affect the oxide formation during the DED process of 316L alloy. Fig. 11(a–b) compares the fracture surface of the 316L samples produced with two different deposition patterns. From this Figure we can see that in both cases some oxides are present in the fracture surface of the samples; red arrows are the oxides rich in Si/Mn and yellow arrows are oxides rich in Si.

Apart from the presence of inclusions in the fracture surfaces which is compatible with those in the as-built microstructures, it is evident that the fracture mode is the typical ductile fracture with fine dimple structure. Moreover, it is revealed that the size of the dimple of the B-0067 samples is markedly larger than that measured on B-0090 sample and this finding is comparable with the PCAS values (see Fig. 8). As can be seen also the plastic deformation near the small oxides (rich in Si) is limited within the boarder of cellular dendrites, while near the lager oxides (reach in Si/Mn) the size of dimples are slightly larger and fracture started from those points because of the fracture propagation.

In order to highlight the role of these inclusions on the tensile behaviour of 316L specimens, the results of this work are compared a previous work from the same authors [40]. Fig. 12 compares the stress-strain curves of three different 316L samples with various oxygen contents. In this graph, the blues curve with 1600 ppm oxygen content is the result of this work using 90° rotation per layer and the other two curves are from the previous work with the same deposition strategy. As can be seen, by decreasing the oxygen content the ductility of the 316L samples improves significantly up to 100%. The fracture surface of those samples which are shown as an inset in Fig. 12 indicate that by increasing the oxygen content the size of oxides markedly increases and therefore play a more detrimental role in the ductility of the 316L samples.

The mechanical properties of the 316L alloy produced in the current research via DED process, in particular, the B-0090 samples are comparable with the previous works with the same deposition patterns (See Table 3). According to previous studies, the fast cooling rates during the AM processes result in a finer microstructure with respect to the microstructure of the components produced via the conventional processes such as forging and casting [40,64].

It is also very interesting to noted that the higher cooling rates also leads to the retention of more residual  $\delta$ -ferrite along the interdendritic regions of 316L samples than can strengthen the soft austenitic matrix. Although, it is reported that the presence of this residual phase deteriorates the ductility of the alloy [66]. Nonetheless, the fracture surface analysis of the samples clearly exhibits that the failure of specimens initiated from the poor interface of matrix and inclusions.

Therefore, it is possible to conclude that the thermal history of the samples, which can be changed by the deposition patterns during the deposition process, plays a key role in the microstructure and mechanical performance of the 316L alloy. However, the presence of inclusion plays the most detrimental role in the fracture toughness of the 316L samples.

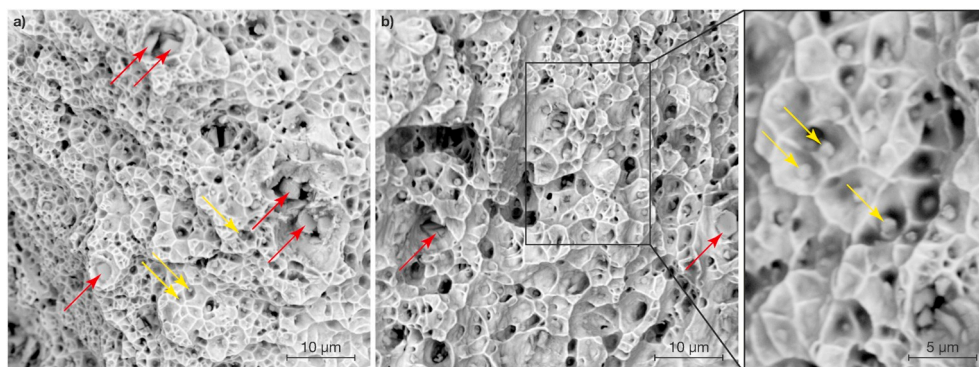


Fig. 11. The typical tensile fracture surface of 316L samples produced with (a) 90°, and (b) 67° rotation per layer.

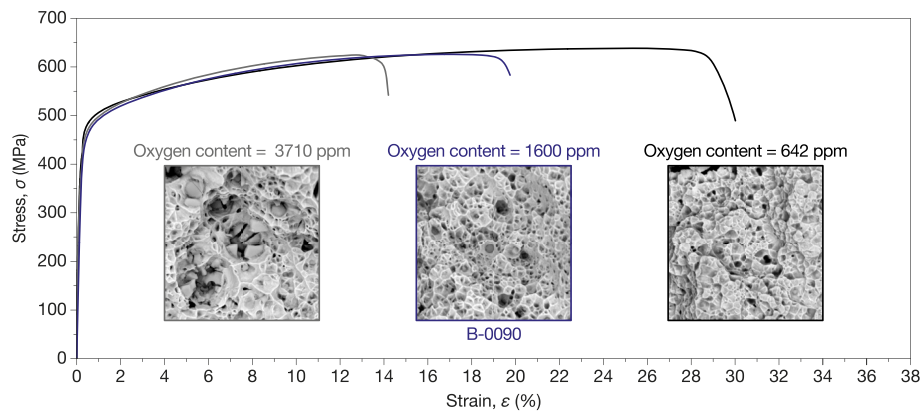


Fig. 12. Stress-strain curves of three different 316L samples with various oxygen contents.

Table 3

Comparison between the mechanical properties of the samples produced in the work with the different production processes.

	YS (MPa)	UTS (MPa)	$\epsilon_r$ (%)	Ref.
DED-67°	469 ± 10	624 ± 10	17 ± 3	Current work
DED-90°	469 ± 6	649 ± 2	23 ± 3	Current work
DED-90°	405–415	620–660	32–40	[38]
SLM	495–500	610–620	38–48	[65]
Wrought	255–310	450	30	[64]
As Cast	262	552	55	[1]

### 3.3. Residual stress

The residual stress state of two different cubes (C-0090-1 and C-0090-2) produced using the 0–90° scanning strategy evaluated on the top surface, on Side A and on Side B is shown in Fig. 13. Fig. 13(a) shows the results obtained on the top surfaces. It is possible to observe an oscillatory trend of residual stresses respect to the depth. It is possible to note that the stress distribution is similar for both cubes. The peak of the curves is obtained approximatively at the same depth (0.8 mm). A difference on the stress distributions is observed at a depth of about 0.4 mm in which the maximum stress of the C-0090-2 sample grows up to 200 MPa. Comparing the direction of principal stress, it is possible to observe that the angle is positive for more than half of the analyzed depth. An abrupt variation on the value of  $\beta$  occurs at a depth of about 0.8 mm for the two samples. This change occurs when the maximum residual stress in the cubes is reached. Fig. 13(b) shows the stress distribution on Side A. The stresses show an oscillatory trend and a similar trend for the two cubes is obtained. For both cubes, the maximum stress is obtained at a depth of about 0.4 mm and after a depth of 0.6 mm, the stresses become almost constant. It is important to observe that the maximum value of stress obtained in C-0090-1 sample is about 3 times higher if compared to the C-0090-2 sample, analogous behaviour was observed at the same depth on the top. In addition, this value overcomes the limit suggested by the standard (80% of yield stress). The trend of the direction of principal stress in the two cubes is almost the same, except for the first two measurements in C-0090-2 sample, in which the  $\beta$  angle is negative. At a depth of about 0.5 mm a variation in the value of the direction of principal stress occurs. It is possible to relate this behaviour to the value of residual stress, that reaches the maximum value at this depth. The results of measurements on Side B, depicted in Fig. 13(c), show an oscillatory trend but it is not possible to identify a tendency. For both cubes, primarily tensile stress is observed, and the maximum stress is about 350 MPa measured at a depth of about 0.3 mm for C-0090-1 sample and at a depth of about 0.8 mm for C-0090-2 sample. Considering the direction of principal stress, it is possible to observe that for C-0090-1 sample, the value of  $\beta$  is mainly positive, with a mean value of 50° instead, for C-0090-2 sample the value of  $\beta$  is predominantly

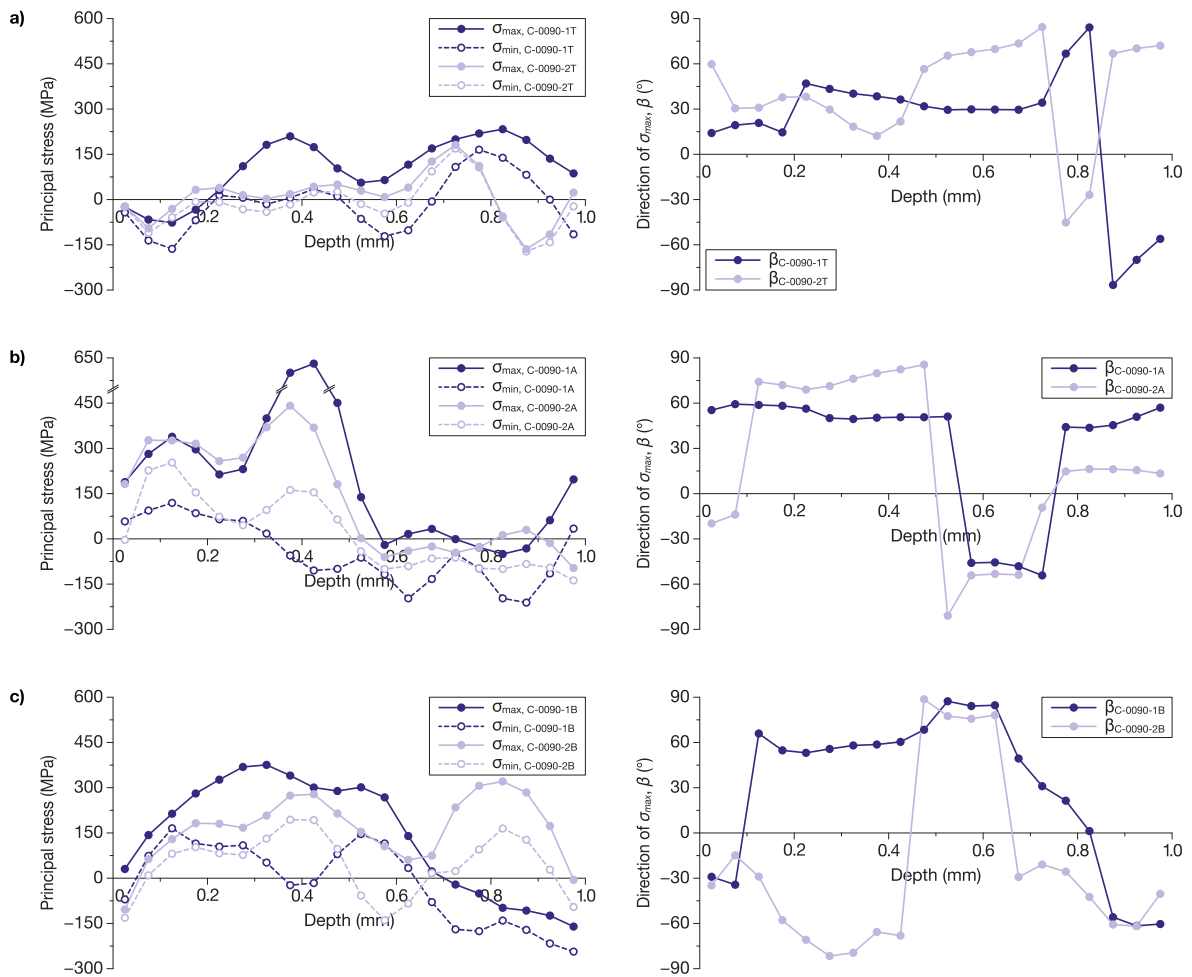
negative. In both cubes, an abrupt variation in the value of  $\beta$  occurs at a depth of about 0.5 mm.

Fig. 14 shows the stress profiles measured on the top surface, on Side A and on Side B of two different cubes (C-0067-1 and C-0067-2) produced using the 0–67° scanning strategy. Fig. 14(a) depicts the stress distribution on the top surface of the C-0067-1 and C-0067-2 samples. The residual stresses exhibit an oscillatory trend but the peaks and the valleys of stress distribution on C-0067-2 sample appear to be shifted of about 0.1 mm with respect to distribution on C-0067-1 sample. The value of residual stress is limited in a small range. For both cubes, the maximum value of stress is about 150 MPa, obtained at a depth of about 0.7 mm for C-0067-1 sample and at a depth of about 0.2 mm for C-0067-2 sample. The shift of the stress distribution is also observed in the trend of the direction of principal stress. For both cubes, the value of  $\beta$  is mainly negative.

The residual stress distribution obtained on Side A for cubes produced using the 0–67° scanning strategy is reported in Fig. 14(b). It is possible to observe that the residual stresses on the analyzed cubes range from –300 to 300 MPa. It is important to note that for both the cubes the measured residual stresses are mainly positive. However, low compressive stress is observed in the subsurface and a compressive peak is located in sample 4 at a depth of 0.7 mm. For both cubes, the direction of principal stress is mainly positive with a mean value of about 50°.

Fig. 14(c) shows the residual stress trend obtained on Side B for cubes built using the 0–67° scanning strategy. The measured stresses show a prevalent tensile state with a maximum value of 300 MPa. After a depth of about 0.7 mm a change in the stress state of C-0067-1 sample is observed. The peaks and the valleys of stress distribution in the two cubes occur approximatively at the same penetration depth. The distribution of  $\beta$  angle in the cubes is almost the same. The direction of principal stress for both cubes is mainly positive and the main value is about 60°.

Table 4 summarizes the measurements of residual stresses on the analyzed cubes. Regarding the direction of principal stresses, it is possible to note abrupt variations, but no specific trend is identified. These variations occur at a depth between 0.4 mm and 0.8 mm. Comparing the value of residual stresses, it is possible to state that using a 0–67° scanning strategy lower residual stresses are obtained. Moreover, it is possible to note that the residual stresses on top surfaces, in both cases, are lower compared to residual stresses obtained on lateral surfaces. This behaviour was attributed to the different cooling rate deriving from the different deposition pattern used in the experimental tests. In particular, higher residual stresses were characteristic of higher cooling rate. In fact, the top surface is characterized by a higher initial temperature and hence by a lower cooling rate. Moreover, the characteristic dimension on the lateral surfaces is related to the layer thickness instead on the top surface the characteristic dimension is referred to hatching distance.



**Fig. 13.** Residual stress depth profiles and direction of the principal stress  $\sigma_{\max}$  (a) on the top surface, and on the lateral surfaces (b) Side A and (c) Side B of the two cubes (C-0090-1 and C-0090-2) produced using the 0–90° scanning strategy.

#### 4. Conclusions

In this study, the effect of two different deposition patterns, 67° and 90° rotation per layer, on the microstructure, inclusion content, cooling rate, PCAS value, mechanical properties and residual stress of 316L stainless steel fabricated via DED process is investigated. Thereafter, the findings in this work is compared with previous works. According to the results in the current work, the following conclusions can be drawn as follow:

1. The general microstructural features of as-built DED samples including the epitaxial growth of columnar grains growing in the direction of maximum thermal gradient in the middle of samples followed by cellular structures in the last layers are revealed in both cases.
2. It is found that by in the samples produced by both two deposition strategies, by increasing the height of sample, the PCAS values increases and at the last layer the PCAS value decreases suddenly due to the changes in the cooling mechanism involved in the solidification at this layer. However, it should be noticed that the variation of PCAS value in the samples using the 67° rotation strategy was not as high as the other samples using 90° rotation.
3. According to the PCAS values, the cooling rates are estimated, and it is revealed that the cooling rate in the samples using 67° rotation strategy was lower than the samples produced by 90° rotation per layer.

4. In both cases, the oxidation phenomena during the deposition were taken place and consequently, these oxides which are mainly rich in Si or Si/Mn deteriorate the mechanical performance of the 316L samples.
5. The calculated average cooling rates in both deposition strategies were found to be in a good agreement with the typical cooling rate reported for DED process.
6. The tensile results of 316L samples confirm that the UTS and elongation of the samples produced by 67° rotation per layer is almost 7% and 27%, respectively, lower with respect to those produced by 90° rotation.
7. The fracture surface analysis revealed that the fracture mode is the typical ductile fracture with fine dimple structure. However, it is found that the size of the dimples of the samples fabricated with lower rotation angle per layer (67°) was markedly larger than another sample using 90° rotation and this finding was comparable with the PCAS values.
8. The role of oxygen content on the elongation to failure of 316L sample was analyzed and compared with the existing works. The outcomes clearly show that by increasing the oxide content the ductility of samples decreases markedly, even down to 50%.
9. The high UTS of DED 316L samples with respect to the conventional production processes such as forging and casting was found to be as a direct effect of higher cooling rates involved in the solidification of the DED samples ( $10^3$ – $10^4$  K/s). In fact, these high cooling rates refine the microstructure and change the phase

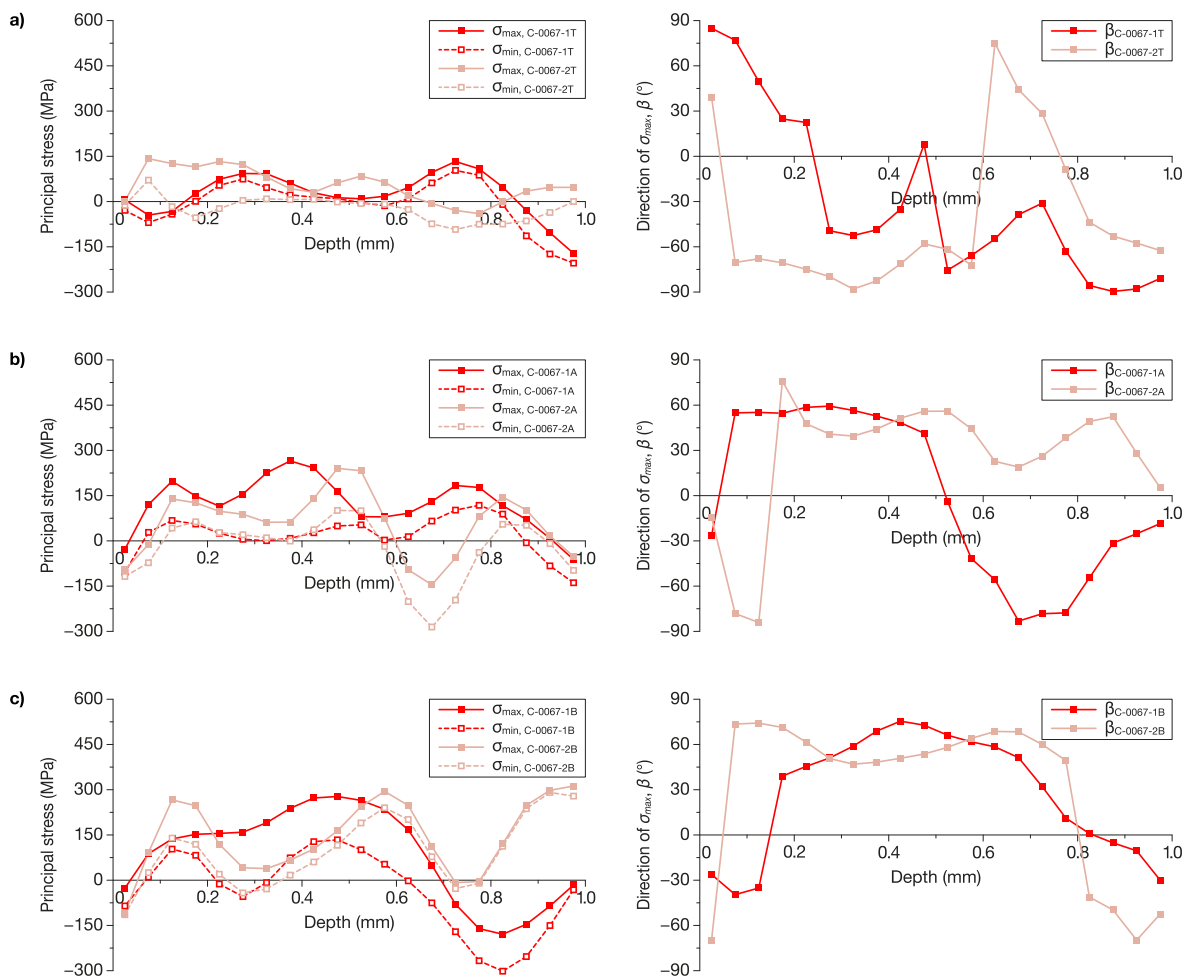


Fig. 14. Stress depth profiles and direction of the principal stress (a) on the top surface, (b) on the Side A lateral surface, and (c) on the Side B lateral surface of the cubes produced using the 0–67° scanning strategy (C-0067-1 and C-0067-2).

Table 4  
Overview of residual stress measurements.

Cube	Principal stress component	Stress (MPa)					
		Top		Side A		Side B	
		min	max	min	max	min	max
C-0090-1	$\sigma_{max}$	-77	233	-50	635	-160	376
	$\sigma_{min}$	-164	165	-211	119	-243	165
C-0090-2	$\sigma_{max}$	-164	181	-97	442	-104	341
	$\sigma_{min}$	-173	169	-138	253	-140	194
C-0067-1	$\sigma_{max}$	-172	133	61	265	-179	278
	$\sigma_{min}$	-204	103	-139	118	-302	134
C-0067-2	$\sigma_{max}$	-40	142	-146	240	-110	312
	$\sigma_{min}$	-92	71	-286	101	-114	291

composition of the final components that improve the mechanical strength of the alloy.

- The residual stress analyses of the cubes indicate clearly that on the top surfaces the residual stresses were similar for both deposition strategies, although higher stress values were observed on the lateral surfaces of the cubes produced using the 90° deposition strategy.

**Declaration of competing interest**

A considerable amount of literature has been published on the correlation between the process parameters and the mechanical properties

of 316L components fabricated via DED process. Nevertheless, neither of referred works considered the effect of deposition pattern on the microstructure, mechanical properties and residual stresses of the 316L components produced by DED process. In fact, to date, this aspect remains unstudied and from the industrial point of view, and thus, there would be an urgent need to understand this aspect to minimize the post-processing cost for stress relieving and also increase the mechanical properties of the parts, simply by changing the deposition pattern. Hence, this work is aimed at better understanding the effect of deposition pattern on the microstructure, mechanical properties and residual stresses of the 316 DED samples.

On the other hand, since in this work include some factors which

affect the microstructure - strength relationships of material and report the changes to mechanical behaviour, is entirely in line with the scope of Materials Science and Engineering A.

### CRedit authorship contribution statement

**Abdollah Saboori:** Conceptualization, Investigation, Validation, Writing - original draft, Writing - review & editing. **Gabriele Piscopo:** Data curation, Investigation, Writing - review & editing. **Manuel Lai:** Resources. **Alessandro Salmi:** Supervision, Formal analysis, Methodology, Writing - review & editing. **Sara Biamino:** Supervision, Writing - review & editing.

### Acknowledgements

The authors would like to acknowledge the European Horizon 2020 research and innovation programme; grant agreement No. 723795/4D Hybrid–Novel ALL-IN-ONE machines, robots and systems for affordable, worldwide and lifetime distributed 3D hybrid manufacturing and repair operations. This work has been partially supported by “Ministero dell’Istruzione, dell’Università e della Ricerca” Award “TESUN-83486178370409 finanziamento dipartimenti di eccellenza CAP. 1694 TIT. 232 ART. 6”. Moreover, the authors would like to knowledge the assistance of Prof. Eleonora Atzeni for her help and support in this research.

### Appendix A. Supplementary data

Supplementary data to this article can be found online at <https://doi.org/10.1016/j.msea.2020.139179>.

### References

- [1] T. Kurzynowski, K. Gruber, W. Stopyra, B. Kuźnicka, E. Chlebus, Correlation between process parameters, microstructure and properties of 316 L stainless steel processed by selective laser melting, *Mater. Sci. Eng.* 718 (2018) 64–73, <https://doi.org/10.1016/j.msea.2018.01.103>.
- [2] M. Aristizabal, P. Jamshidi, A. Saboori, S.C. Cox, M.M. Attallah, Laser powder bed fusion of a Zr-alloy: tensile properties and biocompatibility, *Mater. Lett.* 259 (2020), 126897, <https://doi.org/10.1016/j.matlet.2019.126897>.
- [3] T.J. Hensen, T.G. Aguirre, C.L. Cramer, A.S. Wand, K. Ma, D.A. Prawl, J. D. Williams, T.B. Holland, Additive manufacturing of ceramic nanopowder by direct coagulation printing, *Addit. Manuf.* 23 (2018) 140–150, <https://doi.org/10.1016/j.addma.2018.07.010>.
- [4] A. Saboori, S. Tusacciu, M. Busatto, M. Lai, S. Biamino, P. Fino, M. Lombardi, Production of single tracks of Ti-6Al-4V by directed energy deposition to determine the layer thickness for multilayer deposition, *J. Vis. Exp.* 2018 (2018), e56966, <https://doi.org/10.3791/56966>.
- [5] M. Akbari, R. Kovacevic, An investigation on mechanical and microstructural properties of 316LSi parts fabricated by a robotized laser/wire direct metal deposition system, *Addit. Manuf.* 23 (2018) 487–497, <https://doi.org/10.1016/j.addma.2018.08.031>.
- [6] L.J. Kumar, C.G.K. Nair, Laser metal deposition repair applications for Inconel 718 alloy, *Mater. Today Proc.* 4 (2017) 11068–11077, <https://doi.org/10.1016/j.matpr.2017.08.068>.
- [7] A. Uriondo, M. Esperon-Miguez, S. Perinpanayagam, The present and future of additive manufacturing in the aerospace sector: a review of important aspects, *Proc. Inst. Mech. Eng. Part G J. Aerosp. Eng.* 229 (2015) 2132–2147, <https://doi.org/10.1177/0954410014568797>.
- [8] G. Marchese, S. Parizia, M. Rashidi, A. Saboori, D. Manfredi, D. Ugues, M. Lombardi, E. Hryha, S. Biamino, The role of texturing and microstructure evolution on the tensile behavior of heat-treated Inconel 625 produced via laser powder bed fusion, *Mater. Sci. Eng.* 769 (2020), 138500, <https://doi.org/10.1016/j.msea.2019.138500>.
- [9] I.O. for S. (ISO), *Additive Manufacturing—General Principles—Terminology*, 2015.
- [10] T. DebRoy, H.L. Wei, J.S. Zuback, T. Mukherjee, J.W. Elmer, J.O. Milewski, A. M. Beese, A. Wilson-Heid, A. De, W. Zhang, Additive manufacturing of metallic components – process, structure and properties, *Prog. Mater. Sci.* 92 (2018) 112–224, <https://doi.org/10.1016/j.pmatsci.2017.10.001>.
- [11] W. Liu, J.N. DuPont, Fabrication of functionally graded TiC/Ti composites by laser engineered net shaping, *Scripta Mater.* 48 (2003) 1337–1342, [https://doi.org/10.1016/S1359-6462\(03\)00020-4](https://doi.org/10.1016/S1359-6462(03)00020-4).
- [12] G. Piscopo, E. Atzeni, A. Salmi, A hybrid modeling of the physics-driven evolution of material addition and track generation in laser powder directed energy deposition, *Materials (Basel)* 12 (2019), <https://doi.org/10.3390/ma12172819>.
- [13] A. Saboori, M. Toushekhah, A. Aversa, M. Lai, M. Lombardi, S. Biamino, P. Fino, Critical features in the microstructural analysis of AISI 316L produced by metal additive manufacturing, *Metallogr. Microstruct. Anal.* 9 (2020) 92–96, <https://doi.org/10.1007/s13632-019-00604-6>.
- [14] D. Hu, R. Kovacevic, Sensing, modeling and control for laser-based additive manufacturing, *Int. J. Mach. Tool Manufact.* 43 (2003) 51–60, [https://doi.org/10.1016/S0890-6955\(02\)00163-3](https://doi.org/10.1016/S0890-6955(02)00163-3).
- [15] A. Saboori, A. Aversa, G. Marchese, S. Biamino, M. Lombardi, P. Fino, Application of directed energy deposition-based additive manufacturing in repair, *Appl. Sci.* 9 (2019), <https://doi.org/10.3390/app9163316>.
- [16] M. Franz, J. Bliedner, C. Haupt, Laser metal deposition welding in the field of tool and mould making, *Procedia Eng.* 69 (2014) 237–240, <https://doi.org/10.1016/j.proeng.2014.02.227>.
- [17] A. Saboori, S. Biamino, M. Lombardi, S. Tusacciu, M. Busatto, M. Lai, P. Fino, How the nozzle position affects the geometry of the melt pool in directed energy deposition process, *Powder Metall.* 62 (2019) 213–217, <https://doi.org/10.1080/00325899.2019.1627490>.
- [18] Z. Wang, T.A. Palmer, A.M. Beese, Effect of processing parameters on microstructure and tensile properties of austenitic stainless steel 304L made by directed energy deposition additive manufacturing, *Acta Mater.* 110 (2016) 226–235, <https://doi.org/10.1016/j.actamat.2016.03.019>.
- [19] N.A. Kistler, D.J. Corbin, A.R. Nassar, E.W. Reutzel, A.M. Beese, Effect of processing conditions on the microstructure, porosity, and mechanical properties of Ti-6Al-4V repair fabricated by directed energy deposition, *J. Mater. Process. Technol.* 264 (2019) 172–181, <https://doi.org/10.1016/j.jmatprotec.2018.08.041>.
- [20] I. Gibson, D. Rosen, B. Stucker, Directed energy deposition processes, in: *Addit. Manuf. Technol. 3D Printing, Rapid Prototyping, Direct Digit. Manuf.*, Springer, New York, New York, NY, 2015, pp. 245–268, [https://doi.org/10.1007/978-1-4939-2113-3\\_10](https://doi.org/10.1007/978-1-4939-2113-3_10).
- [21] S.A. Khairallah, A.T. Anderson, A. Rubenchik, W.E. King, Laser powder-bed fusion additive manufacturing: physics of complex melt flow and formation mechanisms of pores, spatter, and denudation zones, *Acta Mater.* 108 (2016) 36–45, <https://doi.org/10.1016/j.actamat.2016.02.014>.
- [22] P.J. Withers, H.K.D.H. Bhadeshia, Residual stress. Part 2 – nature and origins, *Mater. Sci. Technol.* 17 (2001) 366–375, <https://doi.org/10.1179/026708301101510087>.
- [23] K. Dai, L. Shaw, Distortion minimization of laser-processed components through control of laser scanning patterns, *Rapid Prototyp. J.* 8 (2002) 270–276, <https://doi.org/10.1108/13552540210451732>.
- [24] A.H. Nickel, D.M. Barnett, F.B. Prinz, Thermal stresses and deposition patterns in layered manufacturing, *Mater. Sci. Eng.* 317 (2001) 59–64, [https://doi.org/10.1016/S0921-5093\(01\)01179-0](https://doi.org/10.1016/S0921-5093(01)01179-0).
- [25] N. Shamsaei, A. Yadollahi, L. Bian, S.M. Thompson, An overview of Direct Laser Deposition for additive manufacturing ; Part II : mechanical behavior , process parameter optimization and control, *Addit. Manuf.* 8 (2015) 12–35, <https://doi.org/10.1016/j.addma.2015.07.002>.
- [26] G. Piscopo, E. Atzeni, F. Calignano, M. Galati, L. Iuliano, P. Minetola, A. Salmi, Machining induced residual stresses in AlSi10Mg component produced by Laser Powder Bed Fusion (L-PBF), *Procedia CIRP* 79 (2019) 101–106, <https://doi.org/10.1016/j.procir.2019.02.019>.
- [27] A. Salmi, E. Atzeni, Residual stress analysis of thin AlSi10Mg parts produced by Laser Powder Bed Fusion, *Virtual Phys. Prototyp.* 15 (2020) 49–61, <https://doi.org/10.1080/17452759.2019.1650237>.
- [28] A. Salmi, G. Piscopo, E. Atzeni, P. Minetola, L. Iuliano, On the effect of Part Orientation on stress distribution in AlSi10Mg specimens fabricated by laser powder bed fusion (L-PBF), *Procedia CIRP* 67 (2018) 191–196, <https://doi.org/10.1016/j.procir.2017.12.198>.
- [29] A. Salmi, E. Atzeni, History of residual stresses during the production phases of AlSi10Mg parts processed by powder bed additive manufacturing technology, *Virtual Phys. Prototyp.* 12 (2017) 153–160, <https://doi.org/10.1080/17452759.2017.1310439>.
- [30] E.R. Denlinger, P. Michaleris, Effect of stress relaxation on distortion in additive manufacturing process modeling, *Addit. Manuf.* 12 (2016) 51–59, <https://doi.org/10.1016/j.addma.2016.06.011>.
- [31] J. Mazumder, J. Choi, K. Nagarathnam, J. Koch, D. Hetzner, The direct metal deposition of H13 tool steel for 3-D components, *J. Occup. Med.* 49 (1997) 55–60, <https://doi.org/10.1007/BF02914687>.
- [32] M. JD, A. Pinkerton, Z. Liu, I. Manna, L. Li, Microstructure characterisation and process optimization of laser assisted rapid fabrication of 316L stainless steel, *Appl. Surf. Sci.* 247 (2005) 320–327, <https://doi.org/10.1016/j.apsusc.2005.01.039>.
- [33] P. Ganesh, R. Giri, R. Kaul, P. Ram Sankar, P. Tiwari, A. Atulkar, R.K. Porwal, R. K. Dayal, L.M. Kukreja, Studies on pitting corrosion and sensitization in laser rapid manufactured specimens of type 316L stainless steel, *Mater. Des.* 39 (2012) 509–521, <https://doi.org/10.1016/j.matdes.2012.03.011>.
- [34] J.D. Majumdar, A. Pinkerton, Z. Liu, I. Manna, L. Li, Mechanical and electrochemical properties of multiple-layer diode laser cladding of 316L stainless steel, *Appl. Surf. Sci.* 247 (2005) 373–377, <https://doi.org/10.1016/j.apsusc.2005.01.131>.
- [35] X. Wang, D. Deng, M. Qi, H. Zhang, Influences of deposition strategies and oblique angle on properties of AISI316L stainless steel oblique thin-walled part by direct laser fabrication, *Optic Laser. Technol.* 80 (2016) 138–144, <https://doi.org/10.1016/j.optlastec.2016.01.002>.
- [36] M. Ziętala, T. Durejko, M. Polański, I. Kunce, T. Płociński, W. Zieliński, M. Łazińska, W. Stepiński, T. Czujko, K.J. Kurzydłowski, Z. Bojar, The microstructure, mechanical properties and corrosion resistance of 316L stainless

- steel fabricated using laser engineered net shaping, *Mater. Sci. Eng.* 677 (2016) 1–10, <https://doi.org/10.1016/j.msea.2016.09.028>.
- [37] A. Yadollahi, D. Seely, B. Patton, N. Shamsaei, Microstructural features and mechanical properties of 316L stainless steel fabricated by laser additive manufacture, in: 56th AIAA/ASCE/AHS/ASC Struct. Struct. Dyn. Mater. Conf., American Institute of Aeronautics and Astronautics, 2015, <https://doi.org/10.2514/6.2015-1355>.
- [38] M. Ma, Z. Wang, X. Zeng, A comparison on metallurgical behaviors of 316L stainless steel by selective laser melting and laser cladding deposition, *Mater. Sci. Eng.* 685 (2017) 265–273, <https://doi.org/10.1016/j.msea.2016.12.112>.
- [39] X. Wang, D. Deng, H. Yi, H. Xu, S. Yang, H. Zhang, Influences of pulse laser parameters on properties of AISI316L stainless steel thin-walled part by laser material deposition, *Optic Laser. Technol.* 92 (2017) 5–14, <https://doi.org/10.1016/j.optlastec.2016.12.021>.
- [40] A. Saboori, A. Aversa, F. Bosio, E. Bassini, E. Librera, M. De Chirico, S. Biamino, D. Ugués, P. Fino, M. Lombardi, An investigation on the effect of powder recycling on the microstructure and mechanical properties of AISI 316L produced by Directed Energy Deposition, *Mater. Sci. Eng., A* (2019), 138360, <https://doi.org/10.1016/j.msea.2019.138360>.
- [41] K. Zhang, S. Wang, W. Liu, X. Shang, Characterization of stainless steel parts by laser metal deposition shaping, *Mater. Des.* 55 (2014) 104–119, <https://doi.org/10.1016/j.matdes.2013.09.006>.
- [42] A. Saboori, F. Bosio, E. Librera, M. De Chirico, S. Biamino, M. Lombardi, P. Fino, Accelerated process parameter optimization for directed energy deposition of 316L stainless steel, in: Euro PM2018 Congr, Exhebitio, Bilbao (Spain), 2018, pp. 1–6.
- [43] E. ASTM, 837-13a, *Stand. Test Method Determ. Residual Stress. By Hole-Drilling Strain-Gage Method*, 2013.
- [44] F. Yan, W. Xiong, E. Faierson, G.B. Olson, Characterization of nano-scale oxides in austenitic stainless steel processed by powder bed fusion, *Scripta Mater.* 155 (2018) 104–108, <https://doi.org/10.1016/j.scriptamat.2018.06.011>.
- [45] A.O. Kluken, Ø. Grong, Mechanisms of inclusion formation in Al–Ti–Si–Mn deoxidized steel weld metals, *Metall. Trans. A* 20 (1989) 1335–1349, <https://doi.org/10.1007/BF02665492>.
- [46] S.S. Babu, S.A. David, J.M. Vitek, K. Mundra, T. DebRoy, Development of macro- and microstructures of carbon–manganese low alloy steel welds: inclusion formation, *Mater. Sci. Technol.* 11 (1995) 186–199, <https://doi.org/10.1179/mst.1995.11.2.186>.
- [47] A. Saboori, D. Gallo, S. Biamino, P. Fino, M. Lombardi, An overview of additive manufacturing of titanium components by directed energy deposition: microstructure and mechanical properties, *Appl. Sci.* 7 (2017), <https://doi.org/10.3390/app7090883>.
- [48] C. Selcuk, *Laser metal deposition for powder metallurgy parts*, *Powder Met* 54 (2011) 94–99.
- [49] W. Li, M. Soshi, Modeling analysis of grain morphologies in Directed energy deposition (DED) coating with different laser scanning patterns, *Mater. Lett.* 251 (2019) 8–12, <https://doi.org/10.1016/j.matlet.2019.05.027>.
- [50] B. De La Batut, O. Fergani, V. Brotan, M. Bambach, M. El Mansouri, Analytical and numerical temperature prediction in direct metal deposition of Ti6Al4V, *J. Manuf. Mater. Process.* 1 (2017), <https://doi.org/10.3390/jmmp1010003>.
- [51] H.S. Kim, Y. Kobayashi, S. Tsukamoto, K. Nagai, Effect of cooling rate on microstructure evolution of rapidly cooled high-impurity steels, *Mater. Sci. Eng.* 403 (2005) 311–317, <https://doi.org/10.1016/j.msea.2005.05.049>.
- [52] H. Yin, S.D. Felicelli, Dendrite growth simulation during solidification in the LENS process, *Acta Mater.* 58 (2010) 1455–1465, <https://doi.org/10.1016/j.actamat.2009.10.053>.
- [53] J.W. Fu, Y.S. Yang, J.J. Guo, W.H. Tong, Effect of cooling rate on solidification microstructures in AISI 304 stainless steel, *Mater. Sci. Technol.* 24 (2008) 941–944, <https://doi.org/10.1179/174328408X295962>.
- [54] M.H. Farshidianfar, A. Khajepour, A.P. Gerlich, Effect of real-time cooling rate on microstructure in Laser Additive Manufacturing, *J. Mater. Process. Technol.* 231 (2016) 468–478, <https://doi.org/10.1016/j.jmatprotec.2016.01.017>.
- [55] S. Gorsse, C. Hutchinson, M. Gouné, R. Banerjee, Additive manufacturing of metals: a brief review of the characteristic microstructures and properties of steels, Ti-6Al-4V and high-entropy alloys, *Sci. Technol. Adv. Mater.* 18 (2017) 584–610, <https://doi.org/10.1080/14686996.2017.1361305>.
- [56] B. Kocabekir, R. Kaçar, S. Gündüz, F. Hayat, An effect of heat input, weld atmosphere and weld cooling conditions on the resistance spot weldability of 316L austenitic stainless steel, *J. Mater. Process. Technol.* 195 (2008) 327–335, <https://doi.org/10.1016/j.jmatprotec.2007.05.026>.
- [57] P. Guo, B. Zou, C. Huang, H. Gao, Study on microstructure, mechanical properties and machinability of efficiently additive manufactured AISI 316L stainless steel by high-power direct laser deposition, *J. Mater. Process. Technol.* 240 (2017) 12–22, <https://doi.org/10.1016/j.jmatprotec.2016.09.005>.
- [58] P.L. Ferrandini, C.T. Rios, A.T. Dutra, M.A. Jaime, P.R. Mei, R. Caram, Solute segregation and microstructure of directionally solidified austenitic stainless steel, *Mater. Sci. Eng.* 435–436 (2006) 139–144, <https://doi.org/10.1016/j.msea.2006.07.024>.
- [59] S. Atamert, J.E. King, Elemental partitioning and microstructural development in duplex stainless steel weld metal, *Acta Metall. Mater.* 39 (1991) 273–285, [https://doi.org/10.1016/0956-7151\(91\)90306-L](https://doi.org/10.1016/0956-7151(91)90306-L).
- [60] A. Saboori, M. Dadkhah, P. Fino, M. Pavese, An overview of metal matrix nanocomposites reinforced with graphene nanoplatelets; mechanical, electrical and thermophysical properties, *Metals* 8 (2018) 423.
- [61] A. Saboori, S.K. Moheimani, M. Dadkhah, M. Pavese, C. Badini, P. Fino, An overview of key challenges in the fabrication of metal matrix nanocomposites reinforced by graphene nanoplatelets, *Metals (Basel)* 8 (2018) 172, <https://doi.org/10.3390/met8030172>.
- [62] H. Zhang, C. Xu, W. Xiao, K. Ameyama, C. Ma, Enhanced mechanical properties of Al5083 alloy with graphene nanoplates prepared by ball milling and hot extrusion, *Mater. Sci. Eng.* 658 (2016) 8–15.
- [63] R. Casati, M. Vedani, Metal matrix composites reinforced by nano-particles—a review, *Met. (Basel)* 4 (2014) 65–83.
- [64] A. Yadollahi, N. Shamsaei, S.M. Thompson, D.W. Seely, Effects of process time interval and heat treatment on the mechanical and microstructural properties of direct laser deposited 316L stainless steel, *Mater. Sci. Eng.* 644 (2015) 171–183, <https://doi.org/10.1016/j.msea.2015.07.056>.
- [65] R. Casati, J. Lemke, M. Vedani, Microstructure and fracture behavior of 316L austenitic stainless steel produced by selective laser melting, *J. Mater. Sci. Technol.* 32 (2016) 738–744, <https://doi.org/10.1016/j.jmst.2016.06.016>.
- [66] Z. Sun, X. Tan, S.B. Tor, W.Y. Yeong, Selective laser melting of stainless steel 316L with low porosity and high build rates, *Mater. Des.* 104 (2016) 197–204, <https://doi.org/10.1016/j.matdes.2016.05.035>.